

The Kinetic Sunyaev-Zel'dovich effect of the Milky Way Halo

Yuval Birnboim and Abraham Loeb

Harvard Smithsonian CfA, 60 Garden Street, Cambridge, MA, 02138, USA*

(Dated: March 8, 2022)

We calculate the expected imprint of the ionized gas in the Milky-Way halo on the Cosmic Microwave Background (CMB) through the kinetic Sunyaev-Zel'dovich (kSZ) effect. Unlike other Galactic foregrounds, the halo kSZ signature covers the full sky, generates anisotropies on large angular scales, is not accompanied by spectral distortions, and could therefore be confused with primordial CMB anisotropies. We construct theoretical models for various halo components, including smooth diffuse gas, filaments of cold inflowing gas and high velocity clouds. We find that the kSZ effect for all components is above the sensitivity of the *Planck* satellite, over a range of angular scales. However, the typical halo contribution is well below the cosmic variance noise in the primordial CMB power spectrum. High velocity clouds could dominate the halo contribution and better observational data is required to mask them out. We derive expected kSZ maps based on existing data from tracers of the halo gas distribution, such as 21cm maps of neutral hydrogen and H_α maps of recombining gas. The cross-correlation of these maps with the WMAP5 data does not yield any statistically significant signal.

PACS numbers:

Keywords: Cosmic Microwave Background, Milky-Way galaxy

I. INTRODUCTION

The scattering of the Cosmic Microwave Background (CMB) on free electrons with a bulk peculiar velocity relative to the cosmic rest frame, shifts the observed CMB temperature and induces the so-called *kinetic Sunyaev-Zel'dovich (kSZ) effect* [kSZ, 1]. Unlike its thermal counterpart which (for an isotropic distribution of electron velocities) alters the shape of the CMB spectrum, the kSZ effect shifts the spectrum while maintaining its blackbody shape. This makes the kSZ signal on large angular scales a foreground contamination that is indistinguishable from the CMB anisotropies induced at the last scattering surface located at the redshift of cosmological recombination, $z \sim 10^3$.

The removal of the kSZ foreground requires knowledge of the distribution of free electrons and their velocity pattern. A local system of ionized gas that covers the entire sky and is capable of inducing kSZ anisotropies on large angular scales is the halo of our own Milky-Way (MW) galaxy. In this paper, we examine the kSZ signature imprinted by the ionized halo gas. Our primary goal is to find whether this unknown kSZ foreground is an important contaminant which limits our ability to extract the primordial anisotropies on the CMB sky.

The MW galaxy can be modelled as a typical disk galaxy in the concordance Cold Dark Matter (Λ CDM) Universe. Theoretical studies of galaxy formation [2, 3, 4] predict that in the most massive halos with $\gtrsim 10^{12} M_\odot$, the infalling gas is shock-heated to the virial temperature of the halo, where it resides in hydrostatic equilibrium until cooling allows it to drift inwards and make stars in

a central galaxy. This configuration is obtained in hydrodynamic simulations and observed in X-ray clusters. Lower-mass halos are too cold to emit hard X-rays, and it is challenging to observe their soft X-ray emission. The ionized gas in cluster halos causes a kSZ contamination of the CMB which is smaller than its thermal counterpart [5]. Dolag et al. [6] estimated the SZ effect of local large scale structures using constrained realization simulations and found the kSZ to be sub-dominant to the thermal SZ, both peaking at $l \sim 1000$. Suto et al. [7] suggested that the thermal effect of the local group might be detectable in CMB measurements [see, however, Ref. 8, which claims that the assumed local group halo contradicts observations of other galaxy groups]. Other systems of ionized gas, including the intergalactic medium during the reionization era, also provides a negligible contribution on large angular scales [for example, Ref. 9, finds that the kSZ contribution from reionization peaks on the small angular scale of a few arcminutes].

Although the existence of gaseous halos around galaxies is a robust theoretical prediction, its direct observation has so far proven to be challenging [10]. Nicastro et al. [11] and Rasmussen et al. [12] both find evidence of extended halo around the local group containing as much as $10^{12} M_\odot$ and $10^9 - 10^{11} M_\odot$ of gas respectively, by using OVII and OVIII absorption lines (and assuming a metallicity $Z/Z_\odot = 0.3-1$). Other studies used the emission of OVII [13, 14], and the difference between the absorption line strength of the local group and the MW [14] to argue that the gas is more likely to be bound to the MW than the local group. This conclusion is consistent with Sembach et al. [15], Yao et al. [16] which detect OVI lines but do not detect OVII line indicating that the gas is bound to the shallower MW potential well. Hydrodynamic constraints from the interaction between the Magellanic stream gas and the ambient dilute gas predict a non-negligible gaseous halo at a distance

*Electronic address: ybirnboim@cfa.harvard.edu

of ~ 50 kpc from the center of the MW [17, 18]. The existing results (see review in Ref. [19]) are sensitive to uncertain assumptions about the metallicity and the existence of a multi-temperature or multi-component gas. We therefore follow a theoretical approach in modeling the gas in the MW halo and the local group. The latest models [20, 21] of the MW predict that it has a total mass of $M_{\text{virial}} \approx 1 - 2 \times 10^{12} M_{\odot}$, a baryonic mass of $M_{\text{bar}} \leq 2 - 3 \times 10^{11} M_{\odot}$, and a disk+bulge mass of $M_{\text{disk}} \approx 5 \times 10^{10} M_{\odot}$. This allows for a considerable fraction of the total baryonic mass to reside in a gaseous halo, partly in a hot phase at the virial temperature $T \approx 10^6$ K spread out to the virial radius $R_{\text{vir}} \sim 300$ kpc, and partly in a cooler halo component.

Hydrodynamic simulations of galaxy formation predict that the hot MW halo is linked to its cosmological environment and should therefore be highly inhomogeneous. Typically, gas would be accreted into the halo along filaments which are oriented based on the MW’s position within the cosmic web of dark matter and baryons. Following the results presented by Bregman [19] that the MW currently retains its separate halo, we expect filaments to be directed towards the MW’s center rather than the Local group center. The gas in halos of galaxies is not always heated by a virial shock near the virial radius. Birnboim & Dekel [2, 3] showed analytically that the post-shock gas is not always able to support the virial shock. If the halo mass is below some threshold, the post-shock gas is unstable to cooling, and the virial shock cannot propagate outwards. Rather, it remains close to the galactic disk. The threshold mass for metal-poor gas is $\sim 5 \times 10^{11} M_{\odot}$ and for gas at 0.3 of the solar metallicity it is $\sim 10^{12} M_{\odot}$. At high redshifts, halos above this mass threshold originate in rare density peaks, and such halos typically reside in the intersections of filaments within the cosmic web. This allows for denser filaments to avoid shock heating, even if the smooth, diffuse halo hosts a stable virial shock. At $z > 2$, halos above $10^{12} M_{\odot}$ are expected to contain cold flows within filaments embedded in a hot gaseous halo. This picture has been verified by different numerical simulations Kereš et al. [4], Ocvirk et al. [22] and by H_{α} observations [23]. The MW halo is just above the above mass threshold and it contains a hot halo. However, the filamentary structure is still expected to exist, as suggested by Keres et al. [24], who used cosmological *Smooth Particle Hydrodynamics (SPH)* simulations to show that overdense filaments of MW-type halos are more than an order of magnitude denser than the hot diffuse gas in which they are embedded, although 80–90% of the gas remains at the virial temperature.

The hot gas in the MW halo has a cooling time that is shorter than the halo formation time interior to some radius [25] and its central core is expected to cool. Detailed 1D hydrodynamic simulations find, however, that the hot halo component does not cool significantly [26] for some period of time after the initial formation of the virial shock. As the post-shock gas becomes stable, the shock rapidly propagates from the central galaxy to the

edge of the halo, halting the gas infall and, in some cases, putting it in an outward ballistic motion. This causes a complete shutdown of gas accretion which lasts for a few billion years. In the absence of a heating source, cooling would resume after this phase. The unimportance of “hot mode” accretion due to cooling of hot gas and settling to the galactic disk is also seen in 3D simulations of Keres et al. [24]. Mass limits on the galaxy indicate that even if gas had cooled, it did not settle into the galaxy, and would be orbiting the halo as cold clumps [but see Ref. 27, which demonstrated that the formation of cold clumps within the halo via a cooling fragmentation instability is highly unlikely]. In that case, the cold gas in the halo would be partially ionized [28, 29] and yield an even larger signature on the CMB anisotropies.

A different local contribution to the kSZ effect can arise from high velocity clouds (HVCs). While the nature and formation scenarios of HVCs are still under debate [27], we will adopt the inference [30] that HVCs represent compact gas clouds with masses of $10^6 - 10^8 M_{\odot}$. The orbital velocities of HVCs are typically $\gtrsim 100$ km s $^{-1}$ and they are typically found in the vicinity of the galactic plane (at $|z| \leq 10$ kpc (although the latter may very well be an observational selection effect)). Some of these clouds emit H_{α} radiation [17], indicating the existence of ionized hydrogen. The gas is ionized by sources in the Galactic disk, or by hydrodynamical heating (e.g. from the interaction between the Magellanic stream and the hot halo gas [18, 31]). The known distribution of free electrons in the Galactic disk yields a kSZ effect that is mostly confined to a narrow strip of the sky [32, 33], where other Galactic foregrounds (resulting from synchrotron and dust emission) dominate.

In this work we calculate the kSZ effect from the ionized gas in the MW halo, which cover the entire sky. We proceed along two paths. First, we model in §II three halo components: (i) a diffuse hot gas at the virial temperature; (ii) cold filaments; and (iii) high velocity clouds, and then estimate the relative effects of these components on the CMB in §III. Second, we adopt an empirical approach in §IV, and cross-correlate various sky maps of halo gas tracers with the CMB data from WMAP5. Finally, we summarize our results and other possible sources of the kSZ effect in §V.

II. KSZ SOURCES IN THE MILKY-WAY HALO

Before examining the different kSZ components of the Galactic halo, let us obtain a rough estimate for their expected magnitude. The kSZ shift in the CMB brightness temperature is given by [1],

$$\frac{\Delta T}{T} = - \int \frac{v_R(D)}{c} \sigma_T n_e(D) dD, \quad (1)$$

where v_R is the radial peculiar velocity at a distance D along the line of sight (relative to the cosmic rest frame), $n_e(D)$ is the electron number density, c the speed of light

and σ_T is the Thomson cross section. A plausible column density $N_e = 10^{21} \text{ cm}^{-2}$ of halo electrons moving at velocity 600 km s^{-1} (of order the velocity of the MW relative to the CMB) yields a brightness temperature change of $\Delta T/T = 1.2 \times 10^{-6}$, which is detectable in current CMB measurements.

A. The Milky-Way’s invisible halo

The baryonic mass fraction of the MW galaxy is expected to be close to the average cosmic value, $\Omega_b/\Omega_m \approx 0.167 \pm 0.008$ [34], since the MW potential well is sufficiently deep (and the central black hole is of relatively low mass) for feedback to be inefficient in driving baryons out [35]. Using highly efficient feedback, Davé [36] finds that 65% of the gas remains in a MW sized halo. By subtracting the mass of stars and gas in the galaxy, $5\text{--}7 \times 10^{10} M_\odot$ [20, 37], from the total baryonic gas of $\sim 1.5\text{--}3 \times 10^{11} M_\odot$, we infer that the halo gas has a mass of $\gtrsim 10^{11} M_\odot$. Since the halo mass is larger than the critical mass for the formation of a virial shock [2, 3], a hydrostatic halo is expected to form. Detailed cosmological simulations [24] predict that a sub-dominant fraction of the accreted baryons will be accreted in cold filaments which are pressure confined by the hot gaseous halo. This expectation is supported by Kaufmann et al. [28] who find that under some initial conditions the halo gas fragments into cold and hot components, and that most of the gas remains in the halo for 10Gyrs. We assume that at least half of the halo baryons, $5 \times 10^{10} M_\odot$, reside in the hot halo.

We assume that the total mass distribution is described by an NFW [38] profile with $M_{\text{vir}} = 1.5 \times 10^{12} M_\odot$, corresponding to the updated circular velocity of the MW [20, 21]. Based on Refs. [37, 39], we adopt a concentration parameter of $c = 12$. The virial radius for this mass is 296kpc. We consider two models for the halo gas distribution in hydrostatic equilibrium within the dark matter potential: (i) an **isothermal** (constant temperature) profile; and (ii) a generalized NFW density profile [40] with an inner core, in analogy with galaxy clusters [41] and hydrodynamic simulations [42],

$$\rho_{\text{gas}} = \frac{\rho_s}{(1+x)^3}, \quad (2)$$

where $x \equiv rc/R_{\text{vir}}$ and ρ_s is a normalization factor. In the isothermal models, the central density of the gas is set so that the total baryonic mass is encompassed within a radius where the baryonic overdensity is 30 (relative to the cosmic average). For the *core* model, the gas density is normalized so as to give the total amount of assumed mass within R_{vir} , and the temperature profile is fixed by the hydrostatic equilibrium equation. The resulting temperature profile is not far from isothermal, with an overall temperature variation by a factor of 2. Figure 1 shows the density and temperature profiles for the isothermal model (model “*iso*”) with $T_{\text{iso}} = T_{\text{vir}} = 8.1 \times 10^5 K$ (solid red line), $T_{\text{iso}} = 1.2T_{\text{vir}} = 9.7 \times 10^5 K$ (model “*1.2iso*”,

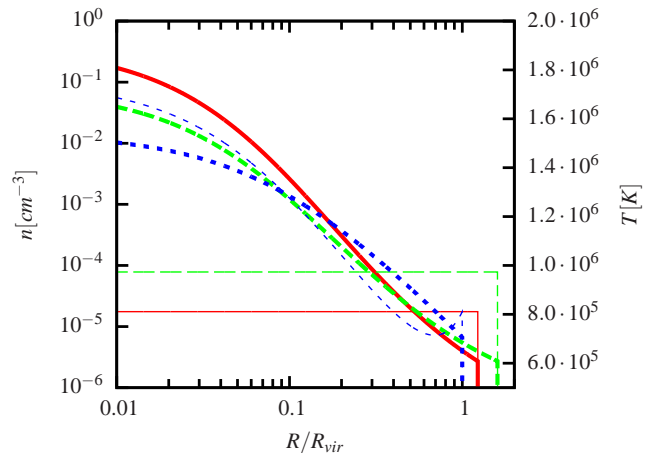


FIG. 1: Density (thick lines) and temperature (thin lines) of the virialized gas in the MW halo for three models: (i) an isothermal profile at the virial temperature T_{vir} (*iso*, solid red line); (ii) an isothermal profile at $1.2T_{\text{vir}}$ (*1.2iso*, long-dashed green line); and (iii) NFW profile with a gaseous core (*core*, dashed blue line). The virial radius is 296kpc.

long dashed green line), and the core model (model *core*, dashed blue line). Although the profiles do not differ much from each other and they all include the same total baryonic mass within R_{vir} , the electron column density of a radial line-of-sight from the center outwards changes significantly between $N_{21} \equiv (N_e/10^{21} \text{ cm}^{-2}) = 4.9, 1.7$ and 0.54 for models *iso*, *1.2iso* and *core*, respectively.

Kaufmann et al. [28] performed detailed SPH simulations of MW-like galaxies based on previous work about cooling-induced fragmentation in galactic halos [29]. They compared the halo cooling and galaxy accretion properties of two MW halo models: one with the gas in an NFW profile (their “*low entropy*” model), and the other with a core profile (“*high entropy*” model), much like our “*core*” model, with a density of $n \approx 10^{-3} \text{ cm}^{-3}$ at a radius of $0.1R_{\text{vir}}$. They have found that while the first model cools the gas too fast, producing a disk with 50% of the total baryonic mass, angular momentum deficiency, and a halo with a too high soft X-ray luminosity, the second model fragments via cooling instability into a configuration of cold clouds embedded within a hot diffuse halo which does not suffer from these problems. A fraction $\sim 10\%$ of the gas remains embedded in the hot halo as HVCs with a predicted covering factor of $\approx 40\%$. The contribution of HVCs to the kSZ signature of the MW halo will be discussed in §II C.

The rotation velocity of the hydrostatic MW halo is expected to be small, and so we assume that the halo is moving at a constant bulk velocity relative to the CMB [43]: $V_{\text{GC-CMB}} = (552.2 \text{ km s}^{-1}, l = 266.5, b = 29.1)$. We assume that the Sun is located at a distance of 8.5kpc from the galactic center [20, 21, 44]. The off-center viewpoint creates a quadropole, and higher spherical harmonics multipoles even for this simple configuration.

B. Filamentary infall into the Milky-Way halo

In the Λ CDM cosmology, dark matter or gas are channeled into galactic halos through filaments which are interconnected to a cosmic web. The gas in the filaments is cold with a temperature in the range $\sim 10^4$ – 10^5 K. As the cold gas enters the galactic halo, its subsequent thermodynamic evolution is determined by its metallicity and the gravitational potential well of its host halo. Previous analytic studies [2, 3] have found that in halos with a virial mass below $10^{12}M_\odot$ and a metallicity of $\sim 0.3Z_\odot$, the gas is expected to fall to the center without shocking. For halos in a range just above this mass threshold at redshifts $z > 2$, a hot gaseous halo is expected to co-exist together with cold, unstable filaments. Detailed cosmological SPH simulations [4] and Eulerian AMR simulations [22] in 3D, have confirmed these expectations. With the MW mass so close to the threshold mass, the filaments are still expected to exist within the MW halo. The confinement of dense infalling filaments within the diffuse halo component was investigated in detail by Keres et al. [24], who have found that the filament gas is overdense by 1-2 orders of magnitude relative to its hot environment and is infalling at ~ 200 km s $^{-1}$. The infalling gas stops at small radii in the vicinity of the galactic disk. Although the MW is expected to be fed by filaments, it is not possible to predict their number, mass flux, and geometry. In this paper, we will assume that there are either one or three filaments, oriented radially towards the Galactic center, each having an infall speed of 200km s $^{-1}$, a conical opening angle of 10° and an overdensity of 10 relative to the ambient hot halo. The direction of these filaments is chosen randomly; this particular choice has little effect on the kSZ power spectrum (§III B).

C. High velocity clouds

High velocity clouds (HVCs) are observed in 21cm HI data [30] as concentrations of gas which are moving at velocities $|V_{LSR}| > 100$ km s $^{-1}$ relative to the local standard of rest (LSR) corresponding to the rotation of the Galaxy. The origin of the HVCs is still debated in the literature. Possible associations include the MW disk [see, e.g. Ref. 45, and references therein], debris from the large or small Magellanic clouds [31], extragalactic origin [27, 30] [but see also Ref. 46, which claims that the 21cm emission originates within a distance of 100 pc]. The distance and ionization fraction of individual clouds (and therefore their size and mass) are unknown. Putman et al. [17] estimated distances of HVCs based on their H_α flux and models for the emission of ionizing radiation from the MW. They find, within the modelling and measurement uncertainties, that most HVCs are within a distance of $\lesssim 30$ kpc. Here we use these results to calculate the inferred electron column densities of HVCs by assuming, for simplicity, that they are spherical homogeneous clouds. For the angular diameter of HVCs on the sky, we

adopt their typical observed diameter, $\theta = 0.2$ rad [based on WHAM and LAB surveys; see Refs. 47, 48]. The total H_α photon flux f (in photons cm $^{-2}$ s $^{-1}$ sr) from a HVC at a distance D and angular diameter θ is obtained from the recombination rate,

$$\pi \left(\frac{\theta}{2}\right)^2 f = \frac{\alpha_B n_e^2 V_{HVC}}{4\pi D^2} \quad (3)$$

where $V_{HVC} = 4\pi/3R_{HVC}^3$ is the volume of the cloud, with $R_{HVC} = D \times \theta/2$ being its physical radius. Here $\alpha_B = 1.17 \times 10^{-13}$ sec $^{-1}$ cm 3 is the case B recombination rate into H_α photons¹. The electron column density through the center of the HVC is,

$$N_e = 2R_{HVC}n_e = \sqrt{\frac{6\pi Df}{\alpha_B}}. \quad (4)$$

In calculating the peculiar velocity of a HVC, we first transform the radial LSR velocity from Putman et al. [17] to the CMB frame of reference, based on the measurements of Kogut et al. [43],

$$V_{HVC-CMB} = V_{HVC-LSR} + V_{LSR-GC} + V_{GC-CMB}, \quad (5)$$

with $V_{HVC-LSR} = v_R \hat{R}$ where \hat{R} is the unit vector in the HVC direction. The velocities have been transformed to Cartesian Galactic coordinates in which the x -axis is oriented towards the Galactic center and the z -axis is oriented perpendicular and out of the galactic plane. In these coordinates, $V_{LSR-CMB} = (-37, -259, 269)$ km s $^{-1}$.

We analyse 25 HVCs from Table 1 of Putman et al. [17] that include all the parameters needed. A more complete inventory of HVCs and their H_α measurements is necessary to produce foreground maps for future CMB experiments. The full contribution of these HVCs to the sky map will be shown in §III but we choose, for illustrative purpose, to consider the values from Putman et al. [17] for a single HVC, “MS1-IIa”, which is a HVC in the Magellanic stream. For this cloud $v_{R-LSR} = -120$ km s $^{-1}$ according to HI measurements and -124 km s $^{-1}$ according to H_α measurements. Converting to the CMB reference frame, the peculiar radial velocity of this HVC is $V_{HVC-CMB} \times \hat{R} = -376$ km s $^{-1}$. For a distance $D = 9.7$ kpc and an H_α flux of $f = 407$ mR = 3.24×10^4 photons cm $^{-2}$ s $^{-1}$ sr, we find $N_e = 1.7 \times 10^{20}$ cm $^{-2}$ and since the reported value of N_{HI} is 1.1×10^{20} cm $^{-2}$ we infer that this cloud is partly ionized. The mass of the cloud is $1.7 \times 10^6 M_\odot$ and its radius is 1 kpc. The kSZ effect on CMB photons passing through the center of the cloud is according to Eq. (1), $\Delta T/T = 1.5 \times 10^{-7}$.

The HVCs of Putman et al. [17] were discovered by the proximity effect of the galactic ionizing radiation. This

¹ We use the table for case B, low density recombination rate from Osterbrock and Ferland [§4.2 of 49] for a gas temperature of 10^4 K.

restricts their detections to the innermost 30kpc around the Galactic disk. Assuming that the origin on these HVCs is extra-galactic, there is no reason to assume that HVCs will only exist near the galactic disk. In addition, a comparison of the baryons in the galaxy and hot halo to the cosmic baryonic fraction of the total halo mass indicates that there are some missing baryons in the MW (§II A, [28, 29]). We therefore construct a synthetic distribution of HVCs. We assume that they trace an isothermal density profile, and include $2.5 \times 10^{10} M_{\odot}$ of mass, distributed as 250 HVCs, with a mass of $10^8 M_{\odot}$ each. Their direction is drawn randomly around the MW’s center, and their distance from the MW is drawn from an isothermal density profile. The velocity has been drawn from a Gaussian distribution with a zero mean and an *rms* value, $\sigma = 100 \text{ km s}^{-1}$. A constant angular size of $\theta = 0.2 \text{ rad}$ is assumed for all HVCs. The constant angular dimension is justified, for example, if the halo had an isothermal profile of gas and the HVCs at a different constant temperature (e.g. 10^4 K) were in hydrostatic equilibrium with the hot halo gas, and the displacement of the observer from the Galactic center is ignored. We have verified that a modest change in the radial distribution and the angular size distribution of HVCs does not change their cumulative kSZ effect considerably.

III. ESTIMATING THE KSZ EFFECT IN THE MW HALO

We generate mock kSZ maps by first constructing a 3D model of the MW halo and then numerically integrating Eq. (1) over lines-of-sights in different directions. The 3D density distribution of the halo electrons is split into a smooth spherically-symmetric component (see §II A), and “objects” which include cold filaments (§II B) and HVCs (§II C). The various versions of the **halo** component are all static and centered around the Galactic center. Their column densities (from the Galactic center to the virial radius) change between 0.5 to $4 \times 10^{21} \text{ cm}^{-2}$ for the “core model” and the “iso model”, respectively. The **filaments** are conical objects, with an opening angle of 10° and an overdensity of 10 with respect to the smooth halo. They are radially infalling at a constant speed of 200 km s^{-1} . Their central column densities are 10 times larger than that of the corresponding halo, but the actual column density (integrated from the Sun) depends somewhat arbitrarily on their location on the sky (see §II B). The **HVCs’** velocity is either taken from observations [17] or chosen randomly to fill the halo (typically $|v_r| 100 \text{ km s}^{-1}$) and they have typical column densities of $\sim 2 \times 10^{20} \text{ cm}^{-2}$ (§II C). The gas density and radial peculiar velocity at specific 3D positions are then integrated along each line-of-sight. We adopt a HEALPix

[50]² pixelization scheme with $N_{\text{side}} = 256$ which provides sufficient resolution for the typical low multipoles ($l < 50$) that we predict (see §III). The resulting kSZ sky maps are then decomposed into spherical harmonics, and the resulting power spectrum is compared to the CMB power spectrum, the cosmic variance noise, and the expected instrumental noise of the *Planck* satellite³. The analysis is performed using the Fortran 90 HEALPix software library.

A. Sky maps

We investigate a few halo profiles as described in Table I. Models 1–3 include only smooth profiles based on the halo models. Models 4 and 5 show the incremental contribution of one filament at Galactic longitude l and latitude b values of ($l = 259^\circ, b = 30^\circ$) (model 4), and of two additional filaments at ($l = 120^\circ, b = 30^\circ$) and ($l = 20^\circ, b = -80^\circ$) (model 5) with respect to the galactic center. The locations of the filaments have been chosen arbitrarily for illustrative purposes. Model 6 adds to model 5 the HVC component according to Putman et al. [17] (§II C) that has a sub-dominant effect relative to the halo and filament contributions. Model 7 described a synthetic HVC population of 250 HVCs with total mass of $2.5 \times 10^{10} M_{\odot}$ as described in §II C. Model 8 is the maximal effect model achieved by combining a hydrostatic *iso* profile, 3 filaments and the synthetic distribution of filaments. The maximal effect of model 8 is $\Delta T/T \sim 8 \times 10^{-6}$, which exceeds the values of $2 \mu\text{K}$ reported by Waelkens et al. [32], Hajian et al. [33] for the Galactic disk. The square of the signal-to-noise ratio is defined as,

$$(S/N)^2 = \frac{1}{(l_{\text{max}} - l_{\text{min}} + 1)} \sum_{l_{\text{min}}}^{l_{\text{max}}} \frac{(2l + 1)C_l}{N_l^{\text{WMAP5}}}, \quad (6)$$

with $l_{\text{min}} = 4$, $l_{\text{max}} = 20$ and N_l^{WMAP5} being the total error estimate of the unbinned WMAP5 data⁴. We show the associated S/N values in the last column of Table I. The models with synthetic HVCs in Table I have $(S/N) \sim 0.2$, making them sub-dominant relative to cosmic variance, although not by much. If the real clouds have a higher column density of electrons than assumed here (e.g. owing to a non-spherical geometry), then their contribution could become noticeable.

Figure 2 shows the kSZ sky maps for a smooth halo model, a halo model with filaments, and a halo model with filaments and HVCs (models 3, 5 and 7, respectively) with the monopole and dipole components owing

² <http://healpix.jpl.nasa.gov>

³ <http://www.rssd.esa.int/index.php?project=planck>

⁴ taken from http://lambda.gsfc.nasa.gov/data/map/dr3/dcp/wmap_tt_spectrum_5yr_v3p1.txt

TABLE I: the kSZ effects of various halo models. In the HVCs column ‘-’, ‘+’, ‘*’ corresponds to no HVCs, HVCs according to Putman et al. [17], and synthetic HVCs, respectively.

#	halo model	number of filaments	HVCs	$\min(\frac{\Delta T}{T})$ [10^{-6}]	$\max(\frac{\Delta T}{T})$ [10^{-6}]	S/N
1	<i>iso</i>	0	-	-3.0	3.5	.030
2	<i>1.2iso</i>	0	-	-0.9	1.0	.006
3	<i>core</i>	0	-	-0.5	0.6	.001
4	<i>core</i>	1	-	-1.0	0.6	.018
5	<i>core</i>	3	-	-1.0	1.1	.041
6	<i>core</i>	3	+	-1.0	1.1	.043
7	<i>core</i>	3	*	-3.0	5.4	.16
8	<i>iso</i>	3	*	-6.1	8.0	.21

to our motion removed. The dipole resulting from the relative velocity of the halo electrons and the CMB is shown.

B. kSZ Power spectra

The power spectrum is recovered from the sky maps by decomposing the sky maps into spherical harmonics, $[\Delta T/T](\theta, \phi) = \sum_{l,m} a_{lm}^{\text{halo}} Y_{lm}(\theta, \phi)$, and averaging over m to obtain $C_l^{\text{halo}} = \frac{1}{2l+1} \sum_m |a_{lm}^{\text{halo}}|^2$ for each l . Figure 4 compares the (binned) power spectra of the 5-year WMAP data [34] to that of models 3,5,6 and 7. For reference, the figure also shows the statistical noise arising from cosmic variance. The figure also presents the expected instrumental noise of the *Planck* satellite,

$$N_l^{\text{exp}} = \langle n_l, n_l \rangle = \Theta_{\text{fwhm}}^2 \sigma_T^2 \exp\{-l(l+1) \frac{\Theta_{\text{fwhm}}}{8 \ln 2}\}, \quad (7)$$

with n_l the noise of each a_{lm} , $\Theta_{\text{fwhm}} = 10'$ the full width at half maximum of the beam and $\sigma_T = 5 \mu K$ being the detector’s sensitivity⁵, and the instrumental noise as reported in the WMAP5 data.

We find that the effect of the ionized MW halo is larger than *Planck*’s instrumental noise for $l \leq 4$. The power spectrum scales roughly linearly with the number of filaments. The filament contribution peaks at $l \sim 15$ and is larger than *Planck*’s instrumental noise for $l \leq 20$. The observed HVC’s contribution to the power spectrum is sub-dominant relative to that of the filaments. The synthetic HVCs contribute to the power spectrum at $l \sim 20$ and are larger than *Planck*’s instrumental noise at $l \leq 40$. A more complete observational census of HVCs with H_α measurements (beyond the 25 HVCs known) will increase the signal linearly in the number of HVCs and improve these constraints. All of the kSZ power spectra lie well

⁵ The values quoted here are reasonable for the 143GHz HFI instrument, <http://www.rssd.esa.int/SA/PLANCK/docs/goal-perf-sum-feb-2004.pdf>

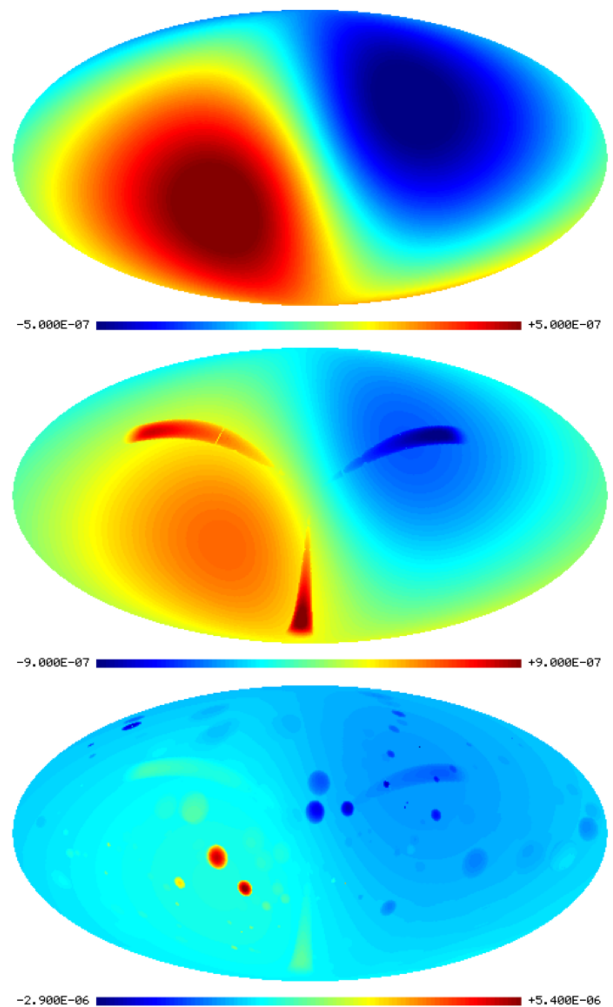


FIG. 2: Fractional changes in the CMB brightness temperature, $\Delta T/T$, from the kSZ effect of various models for the MW halo. All three halo models include a smooth component of the “core” density profile, described in §II A and Fig. 1. *Upper panel*: the smooth core model (model 3). *Middle panel*: core model with three filaments (model 5). *Lower panel*: core model with three filaments and synthetic HVCs (model 7).

below the cosmic variance noise, making them statistically insignificant for the determination of cosmological parameters. All of the models discussed here are below the instrumental noise of WMAP5, and not expected to be observed.

The kSZ contributions from filaments and HVCs are localized and should not in general resemble a Gaussian random field. In an attempt to quantify the non-Gaussianity of the kSZ signal we generated mock CMB maps using the power spectrum of the WMAP5 [34] and superimposed the results of model 7 onto these maps. We then calculated the brightness fluctuations on different angular scales around the HEALPix cell centers and compared a histogram of these to a corresponding histogram of the mock CMB map without the filament

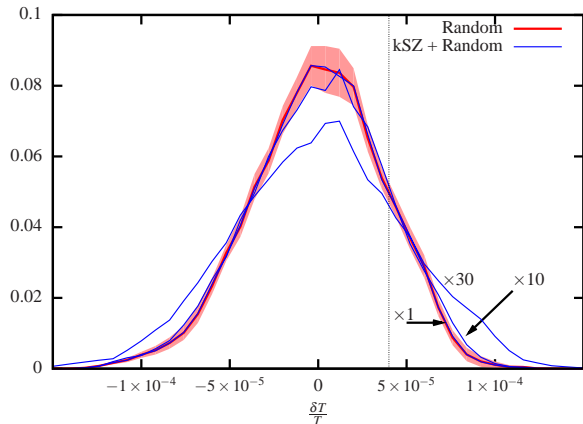


FIG. 3: The one point Gaussianity histogram of random maps, and random maps with model 7 (core, 3 filaments and 250 HVC) superimposed on it. The histogram is generated by polling the average value of δT on disks with diameter 0.15rad. The shaded area is the 1σ scatter of 20 such realizations. The blue lines correspond to the non-Gaussian contribution when model 7 is multiplied by 1, 10 and 30. The normalization is arbitrary.

and HVC contributions. For various choices of the angular scale and the binning intervals, we have found that the non-Gaussian kSZ signature of HVCs and filaments is undetectable. If the number of the HVCs is increased by an order of magnitude, deviations from a Gaussian probability distribution are still virtually non-detectable. Figure 3 compares the non-Gaussianity of model 7, when the kSZ signal is multiplied by factors of 1, 10, and 30. We quantify the strength of the non-Gaussian signal by measuring the “power in the wings” which we define as the ratio between the integral of the histogram beyond some threshold fluctuation amplitude for the non-Gaussian and Gaussian distributions. The cutoff chosen here is $\frac{\delta T}{T} = 4 \times 10^{-5} \text{K}$ (thin vertical line). The power in the wings is: 1.0025, 1.066 and 1.439 for the factors of 1, 10, and 30 respectively. We conclude that if the signal were an order of magnitude larger (a factor of 10 in the column density of the ionized gas or the velocity), then the non-Gaussianity would have been detectable. A more rigorous three-point correlation (f_{NL}) test goes beyond the scope of this paper.

IV. CROSS CORRELATIONS OF HI AND $H\alpha$ MAPS WITH THE CMB

In the previous sections we utilized physically motivated models for the halo gas including filaments and HVCs. In this section we follow an empirical approach and cross correlate various observational maps that might trace the distribution of free electrons in the MW halo. The procedure used here follows the analysis of Land and Slosar [51] for the Leiden/Argentine/Bonn (LAB) Galac-

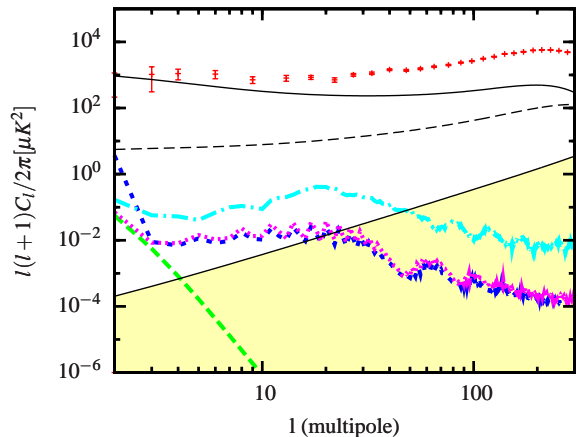


FIG. 4: The CMB WMAP5 power spectrum (red curve with error bars) in comparison to the power spectrum of the *core* halo profile (model 3, long-dashed green line), *core* with 3 filaments (model 5, dotted blue line) and *core* with 3 filaments and HVCs (model 6, purple dashed line) and *core* + 3 filaments + synthetic HVCs (model 7, cyan dot-dashed). The thin solid lines delineate the cosmic variance uncertainties (higher line) and *Planck*'s instrumental noise (lower). The instrumental noise of the WMAP5 data is denoted by the thin, dashed line. Features in the shaded area below the instrumental noise line will not be observable with the *Planck* satellite.

tic HI Survey [52], with the appropriate density/velocity weighting as discussed below. We start by describing the cross correlation of a general sky map (that may cover only part of the sky) with the CMB in §IV A. We then analyse various specific maps and weighting schemes in §IV C.

A. Cross-correlation formalism

We adopt a procedure for cross-correlating a sky map with the CMB data that resembles the one used by Land and Slosar [51], with the important difference that we use a weighting scheme tailored to enhance the kSZ signal. Our procedure is as follows:

- i. Interpolate the sky map into a HEALPix format with $N_{\text{side}} = 512$. HI maps originating from the LAB survey are in fits image format, and so we performed a 2D bilinear interpolation to the coordinates of the center of each HEALPix cell. For $H\alpha$ WHAM maps [47], the original data is presented as scatter plots and we use qshed2d algorithm [53] to interpolate it into HEALPix cell positions.
- ii. Remove the monopole and dipole of the maps by converting the map to (l, m) space and eliminating all the power in $l \leq 1$, and then converting back to real space.
- iii. Combine the mask of the sky map with the

WMAP5 data mask KQ85 [54] to produce the “total mask”, and convolve the total mask with both WMAP data (ILC and V2 map were used) and the sky map.

- iv. Calculate the cross-correlation of the WMAP5 map with the sky map under consideration using the total mask. The auto/cross correlation of maps a and b is given by:

$$C_l^{a,b} = \frac{1}{(2l+1)} \sum_m a_{lm}^a a_{lm}^{*b} \quad (8)$$

and the normalized cross correlation is defined as:

$$C_l^{\hat{a},\hat{b}} = \frac{C_l^{a,b}}{\sqrt{C_l^{a,a} C_l^{b,b}}}. \quad (9)$$

A perfect correlation yields $C_l^{\hat{a},\hat{b}} = 1$, a null correlation yields 0, and a perfect anti-correlation yields a value of -1 for this parameter.

- v. Since the real maps are expected to be non-Gaussian and we expect the nontrivial masks to introduce some correlations between different multipoles, we evaluate the statistical significance of the result by creating random mock CMB maps from the unmasked CMB power-spectrum, and calculating the masked, normalized cross-correlation 10,000 times. The mean and variance of the realizations for each l are then compared to the actual cross-correlation signal.

B. Observed Sky maps

LAB survey: The kSZ weight should depend linearly on the electron column density and the velocity of the ionized gas (Eq. 1). We use data on the neutral hydrogen distribution from the 21cm LAB survey [52, 55, 56, 57], which provides a full sky map of the column density at each velocity bin relative to the LSR. The data is tabulated in bins of 0.5° in angle and a velocity resolution of 1.3 km s^{-1} . The data covers the full sky, and so we use the mask of KQ85 which leaves 82% of the sky unmasked.

The conversion of the measured HI column density N_{HI} to the column density of free electrons N_e requires some model assumptions. We first consider the case where the gas is optically thin to ionizing radiation and is distributed in a spherical shell of a constant width D around the galaxy. Ionizing radiation, either extragalactic or galactic in origin, is impinging on the gas and creating free electrons. In this case, a steady state balance between the recombination and ionization rates imply,

$$n_e^2 D \propto n_{\text{HI}} D \equiv N_{\text{HI}}, \quad (10)$$

with n_e , n_{HI} and N_{HI} denoting the electron density, the HI density and the HI column density, respectively. The

LAB survey maps N_{HI} as a function of velocity and so the sky map LAB1 is constructed as

$$S_{l,b}^{\text{LAB1}} = - \int_v N_{\text{HI}}(l, b, v)^{1/2} v_{\text{CMB}} dv, \quad (11)$$

with $v_{\text{CMB}} = v + V_{\text{LSR-CMB}} \times \hat{r}$, $V_{\text{LSR-CMB}}$ from Kogut et al. [43] and \hat{r} the radius vector to the point of interest (l, b) .

As an alternative case, we assume that the gas is optically thick to ionizing radiation and is collisionally ionized at some constant temperature. In this case,

$$n_e D \propto n_{\text{HI}} D \equiv N_{\text{HI}}, \quad (12)$$

and

$$S_{l,b}^{\text{LAB2}} = - \int_v N_{\text{HI}}(l, b, v) v_{\text{CMB}} dv. \quad (13)$$

Outliers in HI: In addition to cross correlating the full HI LAB data, we also correlated the CMB with a derived map of HVCs and outliers produced by Westmeier [58] by subtracting an HI halo model [59] from the data, and masking all the areas with no extra MW component. The outlier map masks all but 12% of the sky and after convolving this mask with the CMB mask, the total mask leaves 10% of the sky unmasked. The data is expressed in terms of the average velocity and total column density and in analogy with Eqs. (11) and (13) we define models OL1 and OL2 as,

$$S_{l,b}^{\text{OL1}} = -N_{\text{HI}}^{1/2}(l, b) v_{\text{CMB}}, \quad (14)$$

and

$$S_{l,b}^{\text{OL2}} = -N_{\text{HI}}(l, b) v_{\text{CMB}}. \quad (15)$$

H α data: The HI data, while being extremely accurate and detailed, is an indirect tracer of free electrons. A more direct tracer is H α radiation which result from recombinations of electrons and protons. The Wisconsin H-Alpha Mapper [WHAM, 47] provides an H α map of the sky. Above the galactic plane, the WHAM survey has been shown to correlate with HVCs [17]. The WHAM survey covers 73% of the sky and the total mask amounts to 61% of the sky. Assuming, again, some typical width for the H α emitting layer, D , and using Eq. (3), the column density of ionized gas should scale as the square root of the H α flux, $f^{1/2}$, and so we adopt the weighting scheme,

$$S_{l,b}^{\text{WHAM}} = - \int_v f(l, b, v)^{1/2} v_{\text{CMB}} dv. \quad (16)$$

The WHAM data is available as velocity dependent emission measure at scattered locations, and was interpolated to the HEALPix grid following Renka [53].

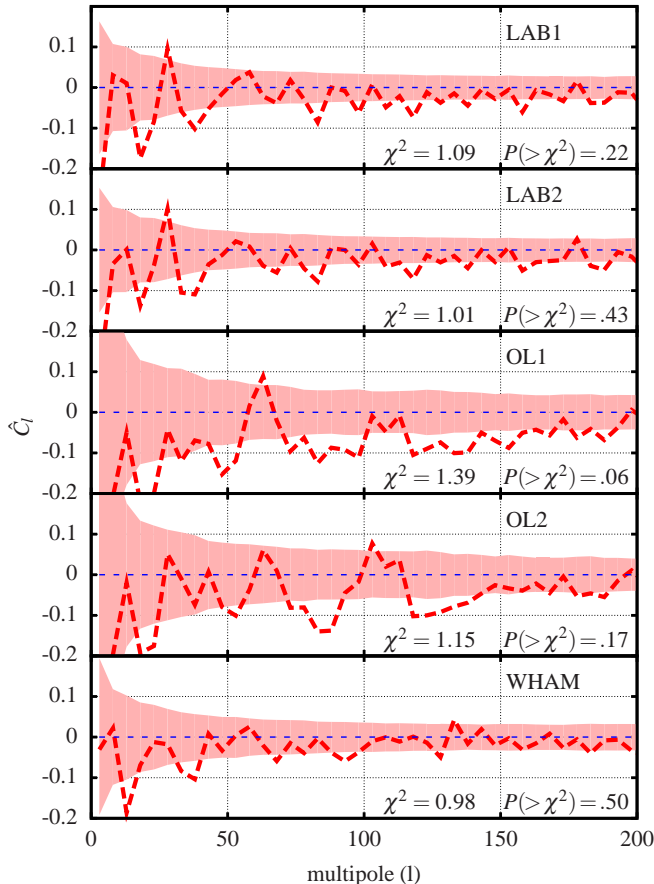


FIG. 5: Normalized cross correlation as a function of spherical harmonic multipoles. We show the full LAB data with LAB1 weighting (Eq. 11, top panel), with LAB2 weighting (Eq. 13, 2nd panel), HVC map with LAB1 (3rd panel), HVC with LAB2 (4th panel), and WHAM with weighting according to Eq. (16). *Solid line*: cross correlation between each map and WMAP5 [34]. *Shaded area*: $1\text{-}\sigma$ scatter levels from 10,000 mock CMB realizations with the WMAP5 power spectrum. Data has been binned to groups of 5 consecutive multipoles in order to reduce the noise level. The χ^2 of the cross correlation and the fraction of mock realizations with χ^2 larger than the real one are marked on each panel.

C. Cross correlation results

Figure 5 shows the normalized cross correlation (Eq. 9) of the sky maps defined in §IV B. The powers here have been binned to groups of 5 l s in order to reduce the noise level. A null cross correlation should have a zero correlation among different multipoles so this averaging should not change the expected (zero) mean of the cross correlation signal. The shaded areas on the plots mark the averaged 1σ regions around averaged means of 10,000 cross correlations for each sky map with a mock CMB map of the same power spectrum. Land and Slosar

[51] have performed a similar analysis on the LAB data, with sky maps of column density of integrals over all or part of velocity space (rather than our expected kSZ weightings), and have found no significant cross correlation. We recover these results here and find for our LAB1 and LAB2 sky maps that there is no apparent cross correlation with the WMAP5 data. A null cross correlation is also consistent with the OL2 and WHAM sky maps.

Sky map OL1 shows an anti correlation larger than 1σ over most multipoles between $50 < l < 200$. The statistical significance of this anti correlation was tested by defining

$$\chi^2 = \frac{1}{(l_{max} - l_{min} + 1)} \sum_{l_{min}}^{l_{max}} \left(\frac{\hat{C}_l}{\hat{\sigma}_l} \right)^2, \quad (17)$$

with $l_{min} = 50$, $l_{max} = 200$ and $\hat{\sigma}_l$ being the standard deviation of 10^4 realization. The χ^2 of the actual data was then compared to the distribution of χ^2 for 10^3 realizations. 6% of the mock realizations had a χ^2 larger than the observed sky map, indicating that such an outcome is not an extremely rare occurrence. Additionally, we performed various tests to eliminate possible biases, including rotation of the OL map by an arbitrary angle (which recovers the null result and eliminates some effects of the mask), and checking different frequency bands of WMAP data (and finding that the ILC and V bands yield almost similar, statistically significant anti-correlation). The anti correlation is probably due to correlations of different multipoles introduced by the nontrivial mask which covers 89% of the sky, while a true kSZ detection should have yielded a positive correlation. We also note that the OL sky maps were derived from the Westmeier [58] maps that were produced by subtracting an HI halo model from the LAB data. An over subtraction could have produced an anti correlation of the type that was found. Finally, the LAB, WHAM and outlier maps have been searched (non-systematically) for features that resemble some of the predicted halo features in §II and no clear correlation was found.

V. DISCUSSION AND CONCLUSIONS

We examined the kSZ effect from the MW halo by first constructing theoretical models for the expected signal, and then adopting an empirical strategy of cross-correlation observed maps of halo gas tracers with the WMAP5 data. Our theoretical models include smooth hot gas, filaments of cold inflowing gas, as well as HVCs. The cross-correlation was analysed for the observed sky maps of HI and H_α emission.

Figure 4 shows that the kSZ signatures from the smooth halo and the filaments declines sharply for multipoles above $l = 4$ and 20, respectively, and is unlikely to be detectable considering the orders of magnitude gap between the signal and the CMB power spectrum. The

contribution from HVCs peaks at $l \sim 20$ with an amplitude which is ~ 3 orders of magnitude lower than the CMB power-spectrum and ~ 2 orders of magnitude lower than the statistical noise of WMAP5. However, for multipoles $l \lesssim 20\text{--}40$, the total kSZ signal from the Galactic halo is expected to be above the instrumental noise of the *Planck* satellite. Galactic foregrounds are being routinely masked or cleaned in the analysis procedure, often based on their unique dependence on photon frequency or Galactic latitude. However, the kSZ effect of the MW halo covers the entire sky and has no frequency dependence relative to the blackbody spectrum, and so its removal cannot be accomplished in the standard linear combination (ILC) maps. The halo effect is larger by an order of magnitude than the kSZ signature of the MW disk [32, 33], and is not confined to a narrow strip around the galactic plane – which is often masked out in a cosmological analysis of the CMB anisotropies. Our theoretical prediction for the HVC contribution to the kSZ effect is based on H_α observations of these HVCs [17] together with a number of model assumptions. In particular, we assume the HVCs to be spherical objects with constant angular size, optically thin, and in ionization/recombination equilibrium with the galactic radiation field. Better understanding of the nature, location and geometry of these HVCs is required for a more robust assessment of their kSZ effect. The modest sample of 25 HVCs with known distances [17] is incomplete, and since the kSZ signal depends linearly on the number of HVCs, a more complete data base is necessary. We estimated the effects of 250 such HVCs by randomly picking them at larger radii. The HVCs are expected to leave a distinct non-Gaussian signature on the CMB sky. Although our preliminary tests have found this signature to be statistically insignificant, the future discovery of more HVCs with known distances might add a non-negligible non-Gaussian contamination to the primordial CMB signal.

The kSZ and thermal SZ effects caused by large scale structures in our local environment has been tested by Dolag et al. [6] using constrained realization simulations. They have found a kSZ signal comparable to the one presented in this paper, but at larger multipoles. The thermal component they predict is even larger. The local group was proposed as a possible source for the thermal Sunyaev-Zel'dovich (tSZ) effect [7]. The early proposals for the dipole and quadropole tSZ amplitudes of the local group are unlikely to be real based on measurements of halos of other galaxy groups [8]. The kSZ signature of the local group would lead to a compact spot in the direction of the Andromeda galaxy (i.e. the direction of the center of mass of the local group), with a diameter of $\sim 20^\circ$. Unfortunately, the detection of this spot is highly challenging.

Our empirically-calibrated sky maps of the kSZ signal are based on the HI data [52], the HI HVCs and outliers distribution [58], and the H_α emission maps [47]. We examined two algorithms for converting HI maps to electron column densities: (i) gas which is optically-thin to ionizing radiation, and (ii) gas with a constant ionization fraction. We have found no statistically significant cross-correlation between the HI and H_α data and the CMB data.

We conclude that the kSZ signal from HVCs imprints patterns on the CMB sky which are detectable but are statistically insignificant in the cosmological context. The kSZ effect could potentially be used to study the content of the Galactic halo. A detection of non-Gaussianity with the spectral features predicted here ($l \leq 20$) would correspond to objects that are either very big or within the local group. Fine tuning of the kSZ effect could be invoked to explain some non-Gaussian features that are seen in the WMAP data. The cold spot [60] can be explained by a dense HVC cloud receding from us at a relatively high speed. The details of such a cloud and the statistical probability that such a cloud exists is left for further investigation.

While cross correlation between various observable sky maps and CMB data is routinely done, we derive here a prescription to estimate the specific contribution from the kSZ effect, that incorporates the column density and velocity in a self consistent way. If a sky map traces the distribution of ionized gas, but its line of sight velocities are not highly correlated, a cross correlation between that map and the CMB will fail to detect the kSZ feature unless the velocities are taken into account in a manner described in §IV. Reversely, a situation in which a sky map convolved according to §IV prescriptions that produces a correlation while the naive luminosity or column density map fails to yield one would indicate that kSZ is observed at high probability. Finally, a more complete future compilation of HVC data could help in creating masks that remove this foreground contamination as well as constrain the unknown physical properties of HVCs.

Acknowledgments

We thank Tobias Westmeier for making the HVC and outlier map available to us digitally, and Matt McQuinn, Anthony Stark and Matias Zaldarriaga for useful discussions and comments. The Wisconsin H-Alpha Mapper is funded by the National Science Foundation. Some of the results in this paper have been derived using the HEALPix [50] package. This work was supported in part by the Harvard University.

[1] R. A. Sunyaev and I. B. Zeldovich, *ARA&A* **18**, 537 (1980).

[2] A. Dekel and Y. Birnboim, *MNRAS* **368**, 2 (2006).

- [3] Y. Birnboim and A. Dekel, MNRAS **345**, 349 (2003).
- [4] D. Kereš, N. Katz, D. H. Weinberg, and R. Davé, MNRAS **363**, 2 (2005).
- [5] J. E. Carlstrom, G. P. Holder, and E. D. Reese, ARA&A **40**, 643 (2002), arXiv:astro-ph/0208192.
- [6] K. Dolag, F. K. Hansen, M. Roncarelli, and L. Moscardini, MNRAS **363**, 29 (2005), arXiv:astro-ph/0505258.
- [7] Y. Suto, K. Makishima, Y. Ishisaki, and Y. Ogasaka, ApJ **461**, L33+ (1996), arXiv:astro-ph/9602061.
- [8] R. A. Pildis and S. S. McGaugh, ApJ **470**, L77+ (1996), arXiv:astro-ph/9608039.
- [9] M. McQuinn, S. R. Furlanetto, L. Hernquist, O. Zahn, and M. Zaldarriaga, ApJ **630**, 643 (2005), arXiv:astro-ph/0504189.
- [10] P. R. Maloney and J. Bland-Hawthorn, ApJ **522**, L81 (1999), arXiv:astro-ph/9907197.
- [11] F. Nicastro, A. Zezas, J. Drake, M. Elvis, F. Fiore, A. Fruscione, M. Marengo, S. Mathur, and S. Bianchi, ApJ **573**, 157 (2002), arXiv:astro-ph/0201058.
- [12] A. Rasmussen, S. M. Kahn, and F. Paerels, in *The IGM/Galaxy Connection. The Distribution of Baryons at $z=0$* , edited by J. L. Rosenberg and M. E. Putman (2003), vol. 281 of *Astrophysics and Space Science Library*, pp. 109+.
- [13] W. T. Sanders, D. Lieu, D. McCammon, L. Rocks, J. E. Vaillancourt, M. Galeazzi, E. Figueroa-Feliciano, R. L. Kelley, R. F. Mushotzky, F. S. Porter, et al., in *Bulletin of the American Astronomical Society* (2002), vol. 34 of *Bulletin of the American Astronomical Society*, pp. 1178+.
- [14] J. N. Bregman and E. J. Lloyd-Davies, ApJ **669**, 990 (2007), 0707.1699.
- [15] K. R. Sembach, B. P. Wakker, B. D. Savage, P. Richter, M. Meade, J. M. Shull, E. B. Jenkins, G. Sonneborn, and H. W. Moos, ApJS **146**, 165 (2003), arXiv:astro-ph/0207562.
- [16] Y. Yao, M. A. Nowak, Q. D. Wang, N. S. Schulz, and C. R. Canizares, ApJ **672**, L21 (2008), 0711.3212.
- [17] M. E. Putman, J. Bland-Hawthorn, S. Veilleux, B. K. Gibson, K. C. Freeman, and P. R. Maloney, ApJ **597**, 948 (2003), arXiv:astro-ph/0307509.
- [18] B. J. Weiner and T. B. Williams, AJ **111**, 1156 (1996), arXiv:astro-ph/9512017.
- [19] J. N. Bregman, ARA&A **45**, 221 (2007), 0706.1787.
- [20] G. Shattow and A. Loeb, MNRAS pp. L133+ (2008), 0808.0104.
- [21] M. J. Reid, K. M. Menten, X. W. Zheng, A. Brunthaler, L. Moscadelli, Y. Xu, B. Zhang, M. Sato, M. Honma, T. Hirota, et al., ArXiv e-prints (2009), 0902.3913.
- [22] P. Ocvirk, C. Pichon, and R. Teyssier, MNRAS **390**, 1326 (2008), 0803.4506.
- [23] R. Genzel, L. J. Tacconi, F. Eisenhauer, N. M. Förster Schreiber, A. Cimatti, E. Daddi, N. Bouché, and et al., Nature **442**, 786 (2006), astro-ph/0608344.
- [24] D. Keres, N. Katz, M. Fardal, R. Dave, and D. H. Weinberg, ArXiv e-prints (2008), 0809.1430.
- [25] S. D. M. White and C. S. Frenk, ApJ **379**, 52 (1991).
- [26] Y. Birnboim, A. Dekel, and E. Neistein, MNRAS **380**, 339 (2007), arXiv:astro-ph/0703435.
- [27] J. Binney, C. Nipoti, and F. Fraternali, ArXiv e-prints (2009), 0902.4525.
- [28] T. Kaufmann, J. S. Bullock, A. H. Maller, T. Fang, and J. Wadsley, ArXiv e-prints (2008), 0812.2025.
- [29] A. H. Maller and J. S. Bullock, MNRAS **355**, 694 (2004).
- [30] L. Blitz, D. N. Spergel, P. J. Teuben, D. Hartmann, and W. B. Burton, ApJ **514**, 818 (1999), arXiv:astro-ph/9803251.
- [31] C. A. Olano, A&A **485**, 457 (2008).
- [32] A. Waelkens, M. Maturi, and T. Enßlin, MNRAS **383**, 1425 (2008), 0707.2601.
- [33] A. Hajian, C. Hernández-Monteagudo, R. Jimenez, D. Spergel, and L. Verde, ApJ **671**, 1079 (2007), 0705.3245.
- [34] G. Hinshaw, J. L. Weiland, R. S. Hill, N. Odegard, D. Larson, C. L. Bennett, J. Dunkley, B. Gold, M. R. Greason, N. Jarosik, et al., ApJS **180**, 225 (2009), 0803.0732.
- [35] A. Dekel and J. Silk, ApJ **303**, 39 (1986).
- [36] R. Davé, ArXiv e-prints (2009), 0901.3149.
- [37] A. Klypin, H. Zhao, and R. S. Somerville, ApJ **573**, 597 (2002).
- [38] J. F. Navarro, C. S. Frenk, and S. D. M. White, ApJ **490**, 493 (1997).
- [39] J. S. Bullock, T. S. Kolatt, Y. Sigad, R. S. Somerville, A. V. Kravtsov, A. A. Klypin, J. R. Primack, and A. Dekel, MNRAS **321**, 559 (2001).
- [40] A. Dekel and Y. Birnboim, MNRAS **383**, 119 (2008), arXiv:0707.1214.
- [41] M. Donahue, D. J. Horner, K. W. Cavagnolo, and G. M. Voit, ApJ **643**, 730 (2006), arXiv:astro-ph/0511401.
- [42] A. Faltenbacher, Y. Hoffman, S. Gottlöber, and G. Yepes, MNRAS **376**, 1327 (2007).
- [43] A. Kogut, C. Lineweaver, G. F. Smoot, C. L. Bennett, A. Banday, N. W. Boggess, E. S. Cheng, G. de Amici, D. J. Fixsen, G. Hinshaw, et al., ApJ **419**, 1 (1993), arXiv:astro-ph/9312056.
- [44] A. M. Ghez, S. Salim, N. N. Weinberg, J. R. Lu, T. Do, J. K. Dunn, K. Matthews, M. R. Morris, S. Yelda, E. E. Becklin, et al., ApJ **689**, 1044 (2008), 0808.2870.
- [45] B. P. Wakker, D. G. York, R. Wilhelm, J. C. Barentine, P. Richter, T. C. Beers, Ž. Ivezić, and J. C. Howk, ApJ **672**, 298 (2008), 0709.1926.
- [46] G. L. Verschuur, ApJ **671**, 447 (2007), 0704.1125.
- [47] L. M. Haffner, R. J. Reynolds, S. L. Tufte, G. J. Madsen, K. P. Jaehnig, and J. W. Percival, ApJS **149**, 405 (2003), arXiv:astro-ph/0309117.
- [48] N. Ben Bekhti, P. Richter, T. Westmeier, and M. T. Murphy, A&A **487**, 583 (2008), 0806.3204.
- [49] D. E. Osterbrock and G. J. Ferland, *Astrophysics of Gaseous Nebulae and Active Galactic Nuclei* (University Science Books, 2006).
- [50] K. M. Górski, E. Hivon, A. J. Banday, B. D. Wandelt, F. K. Hansen, M. Reinecke, and M. Bartelmann, ApJ **622**, 759 (2005), arXiv:astro-ph/0409513.
- [51] K. Land and A. Slosar, Phys. Rev. D **76**, 087301 (2007), 0706.1703.
- [52] P. M. W. Kalberla, W. B. Burton, D. Hartmann, E. M. Arnal, E. Bajaja, R. Morras, and W. G. L. Pöppel, A&A **440**, 775 (2005), arXiv:astro-ph/0504140.
- [53] R. J. Renka, ACM Transactions on Mathematical Software **14**, 149 (1988), ISSN 0098-3500, URL <http://doi.acm.org/10.1145/45054.356231>.
- [54] B. Gold, C. L. Bennett, R. S. Hill, G. Hinshaw, N. Odegard, L. Page, D. N. Spergel, J. L. Weiland, J. Dunkley, M. Halpern, et al., ApJS **180**, 265 (2009), 0803.0715.
- [55] D. Hartmann and W. B. Burton, *Atlas of Galactic Neutral Hydrogen* (Atlas of Galactic Neutral Hydrogen, by Dap Hartmann and W. Butler Burton,

- pp. 243. ISBN 0521471117. Cambridge, UK: Cambridge University Press, February 1997., 1997).
- [56] E. Bajaja, E. M. Arnal, J. J. Larrarte, R. Morras, W. G. L. Pöppel, and P. M. W. Kalberla, *A&A* **440**, 767 (2005), arXiv:astro-ph/0504136.
- [57] E. M. Arnal, E. Bajaja, J. J. Larrarte, R. Morras, and W. G. L. Pöppel, *A&AS* **142**, 35 (2000).
- [58] T. Westmeier, Ph.D. thesis, University of Bonn (2007).
- [59] P. M. W. Kalberla, L. Dedes, J. Kerp, and U. Haud, *A&A* **469**, 511 (2007), 0704.3925.
- [60] P. Vielva, E. Martínez-González, R. B. Barreiro, J. L. Sanz, and L. Cayón, *ApJ* **609**, 22 (2004), arXiv:astro-ph/0310273.